



Mapping of the Ionospheric Total Electron Content over the East African Low–Latitude Region

Geoffrey Cele^{a,*}, Geoffrey Andima^b, Valence Habyarimana^a, Edward Jurua^a

^a Department of Physics, Mbarara University of Science and Technology, Mbarara, Uganda

^b Department of Physics, Busitema University, Tororo, Uganda

Received 3 September 2022; received in revised form 17 November 2022; accepted 3 January 2023

Abstract

Ionospheric behaviour is often monitored using total electron content (TEC) measurements from Global Navigation Satellite System (GNSS) receivers. However, the GNSS receivers are sparse over the East African low-latitude region, resulting in spatio-temporal gaps. In an attempt to address this challenge, the possibility of constructing East African ionospheric maps using Kriging method was investigated in this study. Prior to constructing the maps, the behaviour of the low-latitude ionosphere over this region was characterised using TEC data for 2014 and 2018 during quiet and disturbed conditions. The results show that the highest values of TEC exist between 10:00 UT and 13:00 UT and the minimum values exist at around 03:00 UT. The seasonal trend of TEC reveals that the highest values of TEC occur during March equinox and the lowest during June solstice. The post-sunset TEC often show enhancements between 18:00 UT and 21:00 UT. The enhancements were more pronounced in 2014 than in 2018, especially during the equinoctial months for stations at the crest of the equatorial ionisation anomaly region. These enhancements occurred about an hour earlier at MAL2 than at ADIS during March and September, 2014. The spatial variation of TEC over the East African region was analysed by fitting different semivariogram models. The results reveal that the best semivariogram that describes the spatial variation of TEC over the East African low-latitude region is the Gaussian model. Further analysis shows that the spatial variation of TEC is larger in the meridional direction than in the zonal direction. The Gaussian semivariogram model was then used to construct the TEC maps over the region. The TEC maps were validated using TEC derived from GNSS receivers. The results show very high positive correlation with correlation coefficients between 0.9360 and 0.9970. This suggests that the TEC maps generated by the Kriging interpolation method can be used as good estimates of the GPS-derived TEC at the unmeasured grid points over the region. Therefore, the maps can be used to fill the gaps that exist in the TEC data over the region.

© 2023 COSPAR. Published by Elsevier B.V. All rights reserved.

Keywords: Ionosphere; TEC; Semivariogram; Ordinary kriging; TEC maps

1. Introduction

The ionosphere changes dynamically as a result of the influence of the highly variable sun. Due to its refractive nature, the ionosphere is well known to be the major source of error for the users of satellite based navigation and communication systems because radio signals traversing

through it experience a path delay (Bagiya et al., 2009). This delay depends on the number of free electrons which are present along the signal path from the satellite to the receiver, commonly known as the Total Electron Content (TEC) (Zewdie, 2012) and measured in TEC units (TECU) with 1 TECU equivalent to 1×10^{16} electrons/m². Therefore, TEC is a key parameter to characterise the state of the ionosphere (Norsuzila et al., 2010). The values of TEC have been found to show diurnal, seasonal, and lati-

* Corresponding author.

E-mail address: celegeoffrey@gmail.com (G. Cele).

tudinal variations and depend on solar and geomagnetic activity (Bagiya et al., 2009).

In addition to these variations, the low-latitude ionosphere exhibits other features quite different from those of mid- and high-latitude regions. A double-peaked ionisation structure always appears over the low-latitude region during day time, a phenomenon often referred to as the equatorial ionisation anomaly (EIA) (Appleton, 1946; Hanson and Nagy, 1966). After sunset, ionospheric F region irregularities referred to as the Equatorial Spread F (ESF) occur. Associated with the ESF, is a Pre-Reversal Enhancement (PRE) in the eastward electric field which results in a rapid uplift of the F layer plasma, forming the EIA after sunset (Kelley, 2009).

Both the EIA and the spread F show variations in the time of their peak occurrence and magnitude. The variations are normally explained using the plasma drift theory (Martyn, 1947) and plasma diffusion theory (Mitra, 1946). According to the plasma drift theory, the daytime E-region eastward electric field (\mathbf{E}) which is orthogonal to the terrestrial magnetic field (\mathbf{B}), produces a large upward $\mathbf{E} \times \mathbf{B}$ drift force at the magnetic equator which lifts the plasma to higher altitudes. From the plasma diffusion theory, the lifted plasma diffuses away from the geomagnetic equator due to gravity and pressure gradient forces along the terrestrial magnetic field lines. This leads to the formation of a double-humped structure characterised by a region of depleted ionisation (ionisation trough) at the magnetic equator and two crests of enhanced ionisation at $\sim \pm 15$ to $\pm 20^\circ$ magnetic latitude (Appleton, 1946). The magnitude of $\mathbf{E} \times \mathbf{B}$ drift varies with time of the day, location, seasons, and solar activity. These variations make the TEC over the low-latitude region highly variable on short time scales.

The commonly used source of TEC data is the worldwide network of Global Navigation Satellite System (GNSS) receivers. Unfortunately, these receivers are sparsely and unevenly distributed globally. In addition, often times a number of these receivers experience hardware or software failures leading to spatial and temporal gaps in the recorded data. A modest approach to fill the gaps is through using model generated values. Though various TEC models (e.g. Anderson et al., 1987; Bilitza et al., 2012; Chen et al., 2015; Hajra et al., 2016; Andima et al., 2019) exist, many of the empirical models are constructed basing on hourly, daily, monthly or yearly averages of TEC. Therefore, the TEC models tend to smear out the ionospheric transient features over a region. In an attempt to address the challenge of the models, Global Ionosphere Maps (GIMs) currently provide TEC data that give TEC estimates over the unsampled grids worldwide. However, these maps still have low spatio-temporal resolutions of $5^\circ \times 2.5^\circ \times 1$ h in longitude \times latitude \times time respectively (Grynshyna-Poliuga, 2019), which can not capture peculiar features specific to the region due to their smoothing effect.

To overcome some of the challenges of GIMs, a number of regional TEC maps have been developed using various

interpolation methods; for instance, Inverse Distance Weighted (IDW) interpolation (Jin et al., 2004; Mengist et al., 2016), Multiquadric function (MQ) (Wielgosz et al., 2003), Cubic B-spline (Schmidt et al., 2011), Kriging (KR) interpolation (Orús et al., 2005, 2008, 2019) and Neural Networks (NN) (Arikan et al., 2009). Though deterministic approaches e.g IDW, MQ, NN and Cubic B-spline are relatively simple to implement, they do not capture the spatial structure in the data and therefore not capable of handling sparsely and unevenly distributed data (Grynshyna-Poliuga et al., 2014). Unlike deterministic methods, geostatistical techniques, such as Kriging methods, consider not only the distance between observations but also the spatial structure of the data. They also enable the computation of an error map to spot the locations where the predictions are accurate or flawed (Blanch and Walter, 2002). Due to its robustness, Kriging interpolation is widely applied in environmental sciences (Cressie, 1993).

A number of studies have so far applied Kriging method in ionospheric TEC mapping, for instance, Orús et al. (2005) applied Kriging method to improve the Polytechnic University of Catalonia (UPC) GIMs derived from GPS data, giving birth to UPC Kriging GIMs. They reported that UPC Kriging GIMs improved by standard deviation of 16 % compared to UPC GIMs, using data from several GPS stations distributed worldwide. In another study by Wielgosz et al. (2003), the regional TEC maps obtained using KR and MQ with data from five stations over Ohio state, USA were compared with GIMs of IGS. They reported that both MQ and KR produced similar maps. However, they noted that the TEC level of GIMs is higher by 3–5 TECU, compared to the maps constructed using the KR and MQ methods. They concluded that both KR and MQ were suitable for sparse samplings. Grynshyna-Poliuga (2019) also applied Kriging interpolation method to estimate TEC in the Mid-latitude region of Europe during both quiet and disturbed days. They constructed Kriging TEC maps of $2.5^\circ \times 2.5^\circ$ spatial resolution with a temporal resolution of 15 min and compared them with GIMs from the Center for Orbit Determination in Europe (CODE). They reported that their maps were in good agreement with those of CODE.

Although many regional ionospheric TEC maps have been constructed over other regions, these maps can not be used to capture the dynamics of the East African low-latitude ionosphere. However, in a bid to address this challenge, a few TEC maps have been constructed over the East African region. For instance, Mengist et al. (2016) used IDW interpolation with a spatial resolution of $1^\circ \times 1^\circ$ and a 2 h temporal resolution to map TEC over the East African region. Though their maps captured the formation of EIA over the region, the maps tend to smoothen the ionospheric features of the region due to sparse sampling from fewer IGS stations available. It is then necessary that a more suitable method for sparse sampling be used to capture the spatial variation of the TEC over the region. Therefore, the aim of this paper is to present East African

ionospheric TEC maps constructed using the Kriging technique. The TEC maps are expected to be useful in the estimation of TEC at unsampled or undersampled points over the region.

2. Data and Methods

2.1. Data Sources

This study utilised data from 27 IGS stations within the East African low-latitude region from the years 2014 to 2018, as shown in Fig. 1.

The GPS TEC data sets from 2014 to 2018 in Receiver INdependent EXchange (RINEX) file format for the IGS stations in Fig. 1 were downloaded from University Navstar Consortium (UNAVCO) website¹. The TEC data from the final CODE's GIMs (CODG) were downloaded from CODE's website². Disturbance storm time (Dst) index downloaded from the OMNIWeb Data Explorer website³ was used to identify the geomagnetic storms.

The RINEX data files were processed into TEC data using GPS-TEC analysis software developed at Boston College (Gopi, 2010; Seemala and Valladares, 2011). The software reads raw data in RINEX observation data file (s), and navigation files. The TEC values are derived from the difference of two frequency observables ($f_1 = 1,575.42$ MHz and $f_2 = 1,227.60$ MHz corresponding to L_1 and L_2 GPS bands respectively) from both code and phase observables. The cycle slips in the phase TEC are corrected using the simple arithmetic difference; the differences between adjacent values in phase TEC are checked and the mean difference of the last 20 values is calculated to reduce any noise in the data for lower elevation angles. The differential satellite bias corrections published by University of Bern (<http://ftp.aiub.unibe.ch/CODE/>) were used to remove satellite biases. The differential receiver bias is assumed to be constant for the current day and is solved using the least squares. The final biases are added to Slant TEC (STEC) and the final Vertical TEC (VTEC) values are recalculated by the GPS TEC software (Seemala and Valladares, 2011). A mapping function for a single shell layer model (SLM) (Mannucci et al., 1998) is used to calculate the VTEC assuming an Ionospheric Pierce Point (IPP) height of 350 km (Rama Rao et al., 2006). To minimise undesirable errors due to multipath effect, we used a minimum elevation angle of 30°.

2.2. Methods

2.2.1. The Semivariogram

The semivariogram $\gamma(h)$, is a plot of semivariances as a function of distances, h , between the observations. In order to construct the experimental semivariogram, $\frac{1}{2}n(n-1)$

pairs of combinations were formed from n observations (Pignalberi et al., 2018). The corresponding geospatial lag distances, h , between the pairs of observation locations over the Earth's surface were calculated using Haversine formula [see Eq. 9 in Gade (2010)]. The direction (spatial angle) α of each lag distance, h , from the meridional direction was also determined. The semivariances, $\gamma(h)$ corresponding to the lag distances, h , were then computed (Cressie, 1993) as

$$\gamma(h) = \frac{1}{2} [Z(x) - Z(x+h)]^2. \quad (1)$$

The computed semivariances were binned into K points with the same bin width as explained in Pignalberi et al. (2018). The semivariance corresponding to the K^{th} bin is the mean value $\bar{\gamma}(h)$ of the semivariances within the bin (Cressie, 1993; Deutsch, 1998), given by

$$\bar{\gamma}(h) = \frac{1}{2N(h)} \sum_{i=1}^N [Z(x_i) - Z(x_i+h)]^2, \quad (2)$$

where $Z(x_i)$ and $Z(x_i+h)$ are observed values at locations x_i and (x_i+h) separated by distance h , and $N(h)$ is the number of observation pairs which are a distance h apart within the bin. The experimental semivariogram was obtained by plotting each of the K points of coordinates $(h, \bar{\gamma}(h))$. In this study, we used 20 bins with a bin width of 75 km to model the spatial correlation of TEC over the East African low-latitude region. A theoretical semivariogram model was fitted to the experimental one to ensure continuity in the semivariogram values. The semivariogram parameters (the Sill, the Range and the Nugget effect) were then determined. A typical illustration of the parameters is shown in Fig. 2.

To select the best model, the performance of the semivariogram models: Exponential, Gaussian and Spherical was analysed by fitting each model to the experimental semivariogram using the isotropic assumption. These semivariogram models were further investigated using a random variable Q_1 statistical test (Kitanidis, 1997; Pignalberi et al., 2018). The Q_1 statistical test quantifies the residuals between the values of the model under test and those of the experimental semivariances. The Q_1 test was carried out on all the three semivariogram models for selected disturbed and quiet days. The values of Q_1 were calculated from the residues using the Equation

$$Q_1 = \frac{1}{n-1} \sum_{k=2}^n \frac{\delta_k}{S_k}, \quad (3)$$

where n is the number of observations, $\frac{\delta_k}{S_k}$ are the normalised residues, δ_k are the residues and S_k is the variance of the observations. If the value of Q_1 is close to zero, the validity of the model is not questionable (Kitanidis, 1997). Consequently, the model with the minimum absolute values of Q_1 was selected to be the best and then used to construct TEC maps over the East African low-latitude region.

¹ <http://data-out.unavco.org/pub/rinex/obs/.edu>

² <http://ftp.aiub.unibe.ch/CODE/>

³ <http://omniweb.gsfc.nasa.gov/form/dx1.html>.

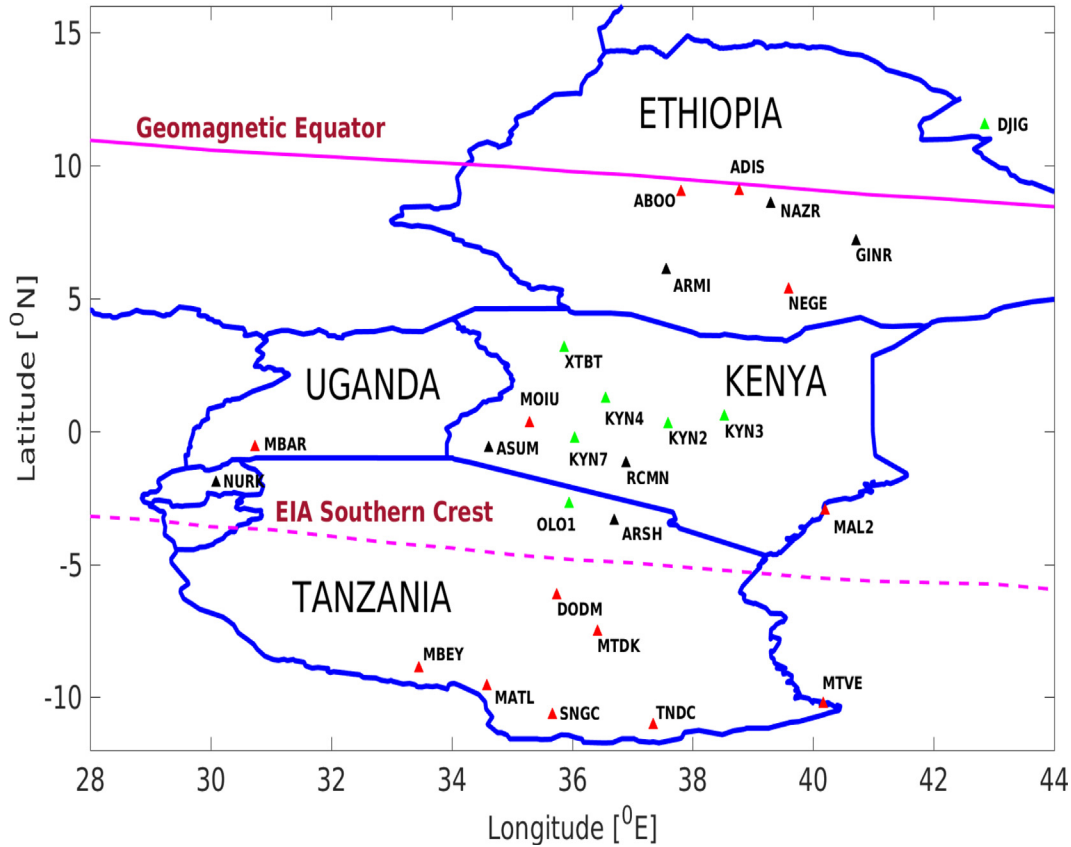


Fig. 1. East African map showing the distribution of IGS stations used in the study. Red triangles represent stations which archived data from 2014 to 2018, black for stations which stopped archiving data before 2018 and green for those which had data after 2014.

To determine the anisotropic nature of the low-latitude ionosphere, the experimental semivariograms were first constructed as earlier discussed. The spatial angles were then binned using the bin width of 30° to obtain a considerable number of grid points in every bin. The centre of the bins were situated at 0° , 30° , 60° , 90° , 120° and 150° , all measured from the meridional direction. Therefore, these angles were taken as the spatial directions during the modelling of the experimental semivariogram. The selected semivariogram model was used to fit the experimental semivariogram in the different spatial directions at a given

time on the selected day. The anisotropic nature of TEC in the low-latitude ionosphere was then investigated by computing the root-mean-squared residues (RMSRes) between the theoretical Gaussian model and experimental semivariogram for the different directions. This was done for some selected international quiet and disturbed days of 2014. The direction that gave the least values of RMSRes for the selected days was taken to be the one that best models the spatial variation of TEC over the East African low-latitude region.

2.2.2. Kriging

The Kriging technique has its origin from a South African mining engineer Daniel Gerhardus Krige, who developed a statistical algorithm to calculate distance-weighted gold grades in South Africa (Matheron, 1963). Kriging method now has a number of variants such as Simple Kriging, Ordinary Kriging, Universal Kriging and Blind Kriging (Lichtenstern, 2013). We used Ordinary Kriging to interpolate GPS TEC over the East African low-latitude region. The choice was based on the fact that Ordinary Kriging prediction uses the stationarity assumption of a constant unknown mean value in the local neighbourhood of each point where the estimate is required, and this could approximate the typical behaviour of TEC in the low-latitude ionosphere.

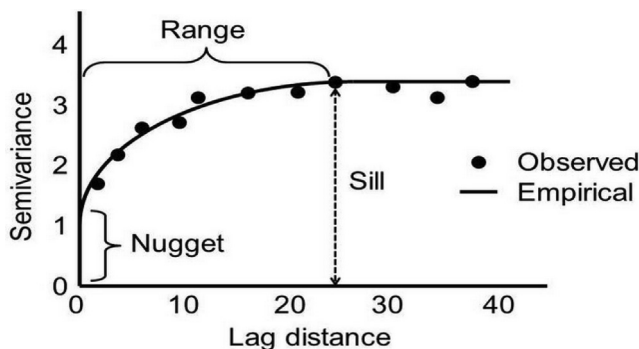


Fig. 2. An example of a semivariogram showing the Range, Sill and Nugget effect. Adapted from Biswas and Si (2013).

The Ordinary Kriging algorithm uses observation values, $Z(x_i)$, and a semivariogram, γ , to determine the unknown values, $Z(x_0)$, at unsampled locations, x_0 , as a linear combination of the known values (Webster and Oliver, 2001; Stanislawski et al., 2002), given by the expression:

$$Z(x_0) = \sum_{i=1}^N \lambda_i Z(x_i), \quad (4)$$

where $Z(x_i)$ is the known value obtained at the known locations x_i (VTEC at IPP grids), N is the number of measured values in the neighbourhood of the estimated value and λ_i is the weight vector which depends on the distance of the estimated value from the measured one.

The Kriging algorithm works on the principle that near points carry more weights than distant ones. The method used to determine the weights is based on minimising the variance

$$\text{var}[Z(x+h) - Z(x)] = 2\gamma(h), \quad (5)$$

where var is the variance operator, γ is the semivariogram, x and $x+h$ are two locations separated by lag distance h .

At each point, Kriging produces a prediction of the variable and the Kriging variance of the prediction by modelling its semivariogram under the assumption that Z is locally stationary (Cressie, 1993). The condition of stationarity means that

$$\sum_{i=1}^N \lambda_i = 1. \quad (6)$$

To impose the unbiased condition, the variance is minimised using Lagrange multipliers (Cressie, 1993).

$$L = \frac{1}{2} E \left[\left(Z(x_0) - \hat{Z}(x_0) \right)^2 \right] - \omega \left(\sum_i \lambda_i - 1 \right), \quad (7)$$

where $E \left[\left(Z(x_0) - \hat{Z}(x_0) \right)^2 \right]$ is the $Z(x_0)$ variance which is expressed in terms of the semivariogram as

$$E \left[\left(Z(x_0) - \hat{Z}(x_0) \right)^2 \right] = 2 \sum_i^N \lambda_i \gamma_{i0}(x_i, x_0) - \sum_i^N \sum_j^N \lambda_i \lambda_j \gamma_{ij}(x_i, x_j). \quad (8)$$

where $i, j = 1, 2, \dots, N$ are the number of unique pairs of observations.

The derivative of Eq. 7 is got with respect to ω and λ_i and equated to zero to obtain the Ordinary Kriging equations in a compact form as

$$\sum_{i=1}^N \lambda_i \gamma_{ij} + \omega = \gamma_{i0}. \quad (9)$$

In matrix form, Eq. 9 is expressed as

$$\begin{bmatrix} \gamma_{11} & \gamma_{12} & \cdots & \gamma_{1N} & 1 \\ \vdots & \vdots & \ddots & \vdots & \vdots \\ \gamma_{N1} & \gamma_{N2} & \cdots & \gamma_{NN} & 1 \\ 1 & 1 & \cdots & 1 & 0 \end{bmatrix} \begin{bmatrix} \lambda_1 \\ \vdots \\ \lambda_N \\ \omega \end{bmatrix} = \begin{bmatrix} \gamma_{10} \\ \vdots \\ \gamma_{N0} \\ 1 \end{bmatrix}, \quad (10)$$

which is in the form $A\lambda = b$.

The weights λ_i can then be determined by solving Eq. 10. The resulting estimation variance is obtained from

$$\sigma_{\text{est}}^2 = b^T \lambda = b^T A^{-1} b, \quad (11)$$

where A is the matrix containing the semivariogram estimates for the measured values, λ is the vector that contains the weights λ_i and the Lagrange multiplier ω , and b is the vector which has the semivariogram predictions for the unmeasured values at known grid points (Grynshyna-Poliuga et al., 2014).

The semivariograms and the TEC maps in this study were constructed using the Kriging toolbox downloaded from website ⁴. The semivariogram parameters which include: the Range, a , Sill, s , and Nugget effect, γ_0 , were used as inputs to solve the Kriging Eq. 10. The solutions to the Kriging equation gave the Kriging weights, λ_i , which were used to predict VTEC at unknown locations in the neighbourhood of the measured VTEC values at a given time as in Eq. 4. It is important to note that the weights are time-dependent and so were estimated every time prior to construction of the corresponding TEC map. The measured VTEC values obtained at IPPs at any time were interpolated using the calculated weights in order to predict the values of VTEC at unmeasured locations at that instant. These predictions were then mapped over the East African region with a spatio-temporal resolution of $1^\circ \times 1^\circ \times 6$ min in latitude \times longitude \times time.

3. Results and Discussions

3.1. Diurnal and Seasonal Variation of TEC over East Africa

The diurnal, seasonal and solar activity variation of TEC over the East African region was studied using TEC data from the IGS stations ADIS located within the trough and MAL2 located at the southern crest of the EIA. These stations were chosen because they lie nearly along the same longitude, and therefore the local time effects are considerably minimised. Data for the equinox (March and September) and solstice (June and December) months were used to characterise the variation of TEC with seasons. Fig. 3 shows the variation of the monthly averaged TEC at ADIS (red curve) and MAL2 (blue curve) during the years 2014 and 2018. The diurnal trend over this region shows an increase in the values of TEC from minimum between 02:00 UT and 04:00 UT to maximum between 10:00 UT and 13:00 UT and then a decrease to a minimum after sun-

⁴ <https://sourceforge.net/projects/mgstat/files/mGstat/>.

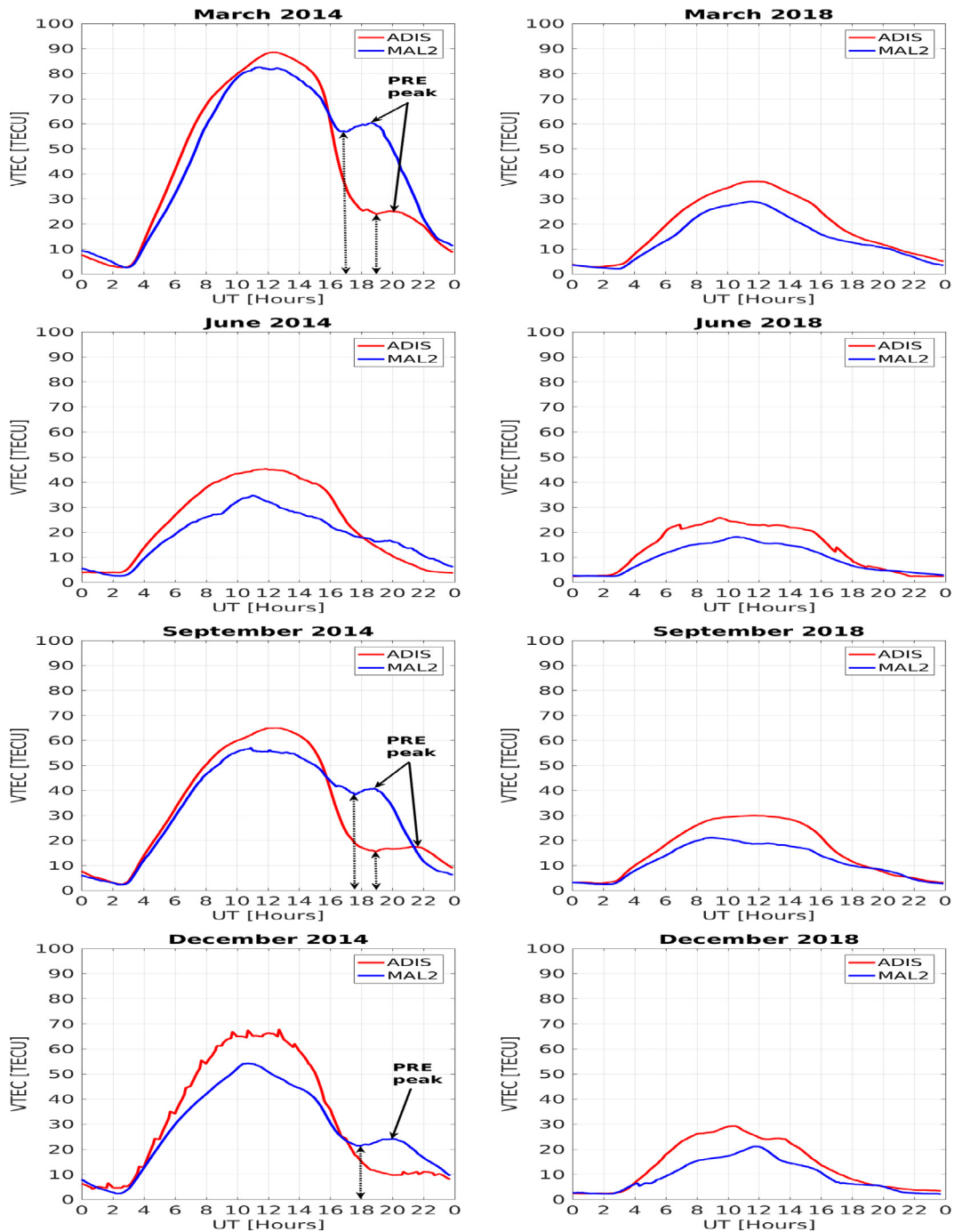


Fig. 3. Variation of TEC at ADIS and MAL2 during March, June, September and December of 2014 and 2018.

set in both years of 2014 and 2018. During the day, TEC values are higher at ADIS than at MAL2. A similar trend was reported before (e.g. Tariku, 2015; Hajra et al., 2016; Olwendo et al., 2016; Sulungu et al., 2018). The diurnal TEC trend is influenced by the rate of photoionisation and this rate depends on solar zenith angle and solar activity. In 2018, TEC remained higher at ADIS than MAL2 during the selected months. However in 2014, this observation was true only from about 03:00 UT to about 16:00 UT and after which the trend was observed to reverse, where

the values of TEC were higher at MAL2 than ADIS. The change in trend is attributed to the high solar flux during 2014 that resulted in an enhancement in the EIA development, which is not the case with the low solar activity (LSA) year 2018.

The seasonal pattern shows that the maximum TEC values occur during equinoxes, and minimum during June solstice. A plausible explanation to this observation is that during the equinox months, the sub-solar point is near the equator, where the eastward electric field often becomes

larger, and this increases the intensity of the fountain effect which controls the level of ionisation at the equator (Olowendo et al., 2016). In solstices, the sub-solar point moves to higher latitudes, the fountain effect is expected to reduce and consequently the ionisation peaks during the solstices decrease. The seasonal trend exhibits equinoctial asymmetry of TEC over the East African low-latitude, where March equinox recorded higher TEC values than September equinox. The equinoctial asymmetry at low latitudes can be explained in terms of the global thermosphere circulation (Bailey et al., 2000).

Well developed post sunset (secondary) TEC peaks were observed during high solar activity (HSA) year of 2014 for the months of March, September and December between 18:00 UT and 21:00 UT, with March equinox featuring the most prominent post sunset peak, followed by September equinox and the least was observed during December solstice. During HSA period, the pre-reversal enhancements in the eastward electric field are sufficient to influence any night-time enhancement in TEC over the low-latitude region (Tariku, 2015). The post sunset peak values of TEC over MAL2 were higher than those over ADIS for all the selected months. The higher values of TEC over MAL2 than over ADIS at post sunset is attributed to the effect of the upward $\mathbf{E} \times \mathbf{B}$ drift force leading to an enhancement in TEC at the crest region (Olowendo et al., 2016). The highest PRE peak value over MAL2 was recorded during March equinox (~ 60 TECU), followed by September equinox (~ 40 TECU) and the least during June solstice (~ 17 TECU). During equinox of 2014, PRE occurred 1 h earlier at MAL2 (at about 19:00 UT) than ADIS (at about 20:00 UT). The difference of 1 h in the time of occurrence of PRE during the equinoctial months of 2014 could be as a result of the latitudinal difference. A study by Ghosh et al. (2020) indicated that the F-region winds control the PRE peak through the F-region dynamo mechanisms, accompanied by E- and F-region coupling processes. The PRE develops as a result of the reversal in the F-region zonal wind which results in an additional upward current where the E-region pedersen conductivity is reducing at post sunset (Heelis et al., 2012). The results further show that the TEC values at the crest regions were higher than those at the dip equator after sunset for the selected months of 2014, which is similar to the findings from the study by Olowendo et al. (2016) over this region. The LSA year 2018 registered extremely weak or no PRE for the selected months of the year. A similar observation was reported by Tariku (2015) who studied the variation of GPS TEC over Ethiopia during both low and high solar activity periods from 2008–2009 and 2012–2013 respectively.

3.2. Spatial Variation of TEC

3.2.1. Selection of a Semivariogram Model

Spatial TEC variance was used to study the variation of TEC over the East African low-latitude region. Fig. 4

shows Exponential, Gaussian and Spherical fits on quiet and disturbed days, for instance, DOY 245 and 255 of 2014.

The performance of the semivariogram models in fitting the experimental semivariogram constructed using TEC was analysed using the Q_1 statistical test (Kitanidis, 1997; Pignalberi et al., 2018).

Table 1 shows the results for the Q_1 statistical test on the semivariogram models during quiet and disturbed days. For example, during the quiet DOY 048 and 254 of 2014, the highest $|Q_1|$ value of 0.032 was obtained with the Spherical model, while the smallest was with the Gaussian model. Similarly, on the disturbed DOY of 050 and 255 of 2014, the highest value of 0.0181 was obtained with the Spherical model while the smallest value was recorded by the Gaussian model. As earlier mentioned, the best model is the one that produces the smallest value of $|Q_1|$. Therefore, the Gaussian semivariogram was selected as the model that best describes the spatial variation of TEC observations over the East African low-latitude region.

3.2.2. Directional Variation of TEC

The angle dependence of the TEC variation was studied using the Gaussian semivariogram model. The TEC variances were binned in the directions of 0° , 30° , 60° , 90° , 120° and 150° , all measured clockwise from the meridional direction, and the resulting experimental semivariograms were then fitted to the Gaussian model. Fig. 5 shows the spatial variation of TEC in different spatial directions using the gaussian semivariogram on DOY 257 of the year 2014 at 12:00 UT.

The observation from Fig. 5 is that on DOY 257 at 12:00 UT, the spatial variation of TEC in the meridional direction is larger than that in the zonal direction. The larger TEC variation in the meridional direction could be caused by the equatorial ionisation anomaly. The anomaly is as a result of the plasma uplift to higher altitude and then diffusion of the plasma on either side of the magnetic equator, forming double humps with a region of depleted plasma in the ionosphere over the magnetic equator. Therefore, the larger variation of TEC in the meridional direction is attributed to the plasma diffusion in this direction. On the other hand, the spatial angle of 90° corresponds to the zonal direction where TEC values are close to each other (having no big variation). The TEC values are close because there is no mechanism to influence the electron density variation in the zonal direction, apart from the zonal wind whose impact could be negligible within a small longitudinal range scale. Therefore, the horizontal line in Fig. 5 shows that the TEC variances are independent of the lag distance over a small region like East Africa. As a result, the Gaussian model does not fit the variances well in this direction as these variances are not correlated with the lag distances.

The anisotropic nature of the East African ionosphere was further investigated by computing the RMSRes between the theoretical Gaussian model and experimental

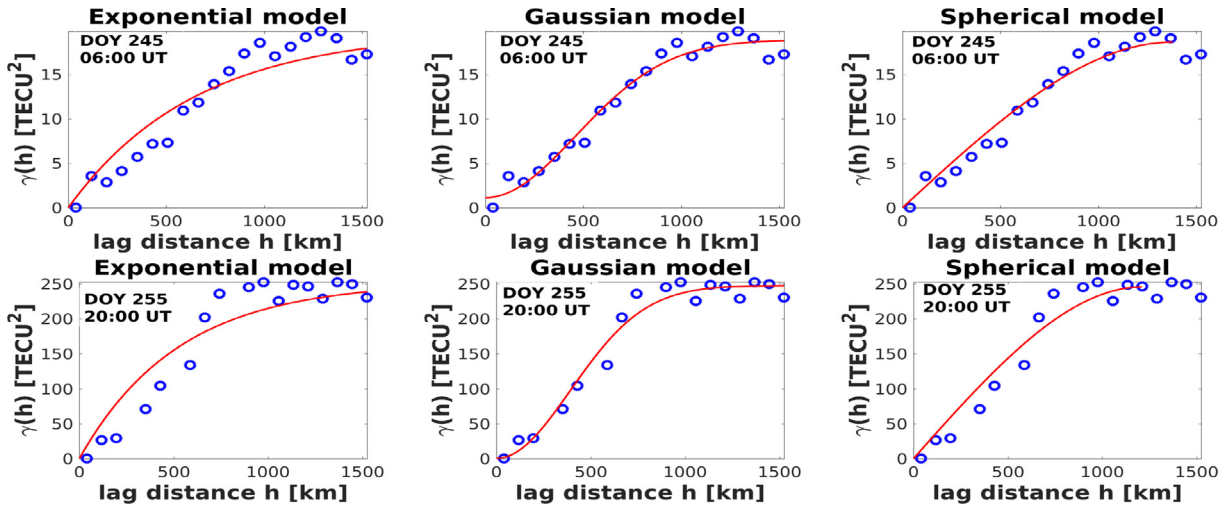


Fig. 4. A typical example of Exponential, Gaussian and Spherical semivariogram models used to fit the TEC variances over East African region on a quiet DOY 245 (top row) and a geomagnetically disturbed DOY 255 (bottom row) of 2014. The blue circles are the observations and the red curves represent the modelled values.

Table 1

The Q_1 statistical test results for the Exponential, Gaussian and Spherical semivariogram models on quiet DOY 048, 254 and disturbed DOY 050, 255 at 11:00 UT.

| Semivariogram model | Quiet DOY | $ Q_1 $ | Disturbed DOY | $ Q_1 $ |
|---------------------|-----------|----------|---------------|----------|
| Spherical | 048 | 0.0320 | 050 | 0.0181 |
| Gaussian | | 1.160e-6 | | 4.930e-7 |
| Exponential | | 0.0180 | | 0.0091 |
| Spherical | 254 | 0.0265 | 255 | 0.0042 |
| Gaussian | | 2.962e-6 | | 4.271e-7 |
| Exponential | | 0.0089 | | 0.0039 |

semivariogram for the different spatial angles of 0° , 30° , 60° , 90° , 120° and 150° . This was done for two international quiet (DOY 048 and 257) and disturbed (DOY 050 and 054) days of 2014. Table 2 shows the RMSRes values obtained using the Gaussian model. From the results in Table 2, the spatial angle of 0° consistently produced the least values of RMSRes for all the selected days. The smaller the residuals the closer the experimental values to the model values and the better the model in fitting the experimental semivariogram. Therefore using the Gaussian model, the spatial angle of 0° was chosen as the direction that gives the best autocorrelation of TEC over the East African low-latitude region.

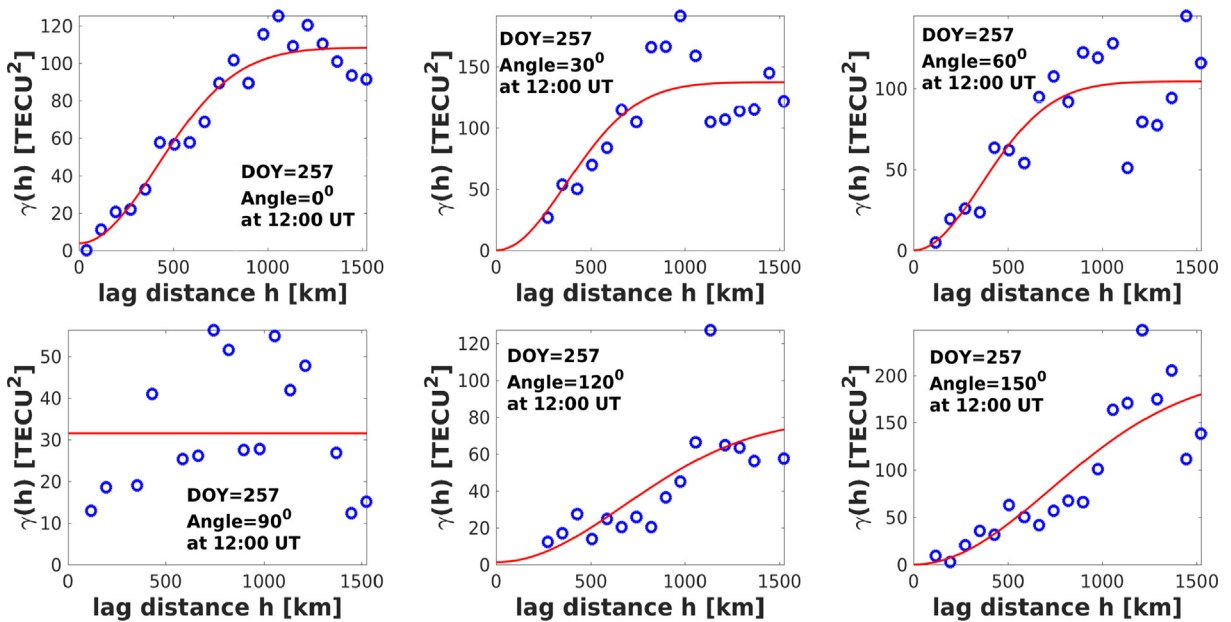


Fig. 5. Spatial variation of TEC in different directions over the East African low-latitude region using the Gaussian semivariogram model on a typical quiet DOY 257 of 2014 (14–09-2014) at 12:00 UT. The blue circles represent observations and the red curve represents the modelled values.

Table 2

Variation of the Root-Mean-Squared Residuals (RMSRes) of TEC over the East African ionosphere using Gaussian semivariogram model. The values of the RMSRes in square TEC units were calculated at 16:00 UT under quiet and disturbed conditions.

| Quiet DOY | Angle [Deg.] | RMSRes [TECU ²] 16 : 00UT | Disturbed DOY | Angle [Deg.] | RMSRes [TECU ²] 16 : 00UT |
|-----------|--------------|---------------------------------------|---------------|--------------|---------------------------------------|
| 048 | 0 | 2.2977 | 050 | 0 | 2.9970 |
| | 30 | 5.1115 | | 30 | 3.6915 |
| | 60 | 2.3174 | | 60 | 4.1293 |
| | 90 | 5.1634 | | 90 | 6.1921 |
| | 120 | 2.3000 | | 120 | 5.8148 |
| | 150 | 3.6970 | | 150 | 4.0955 |
| 257 | 0 | 5.1891 | 054 | 0 | 6.2074 |
| | 30 | 5.5267 | | 30 | 7.2086 |
| | 60 | 6.4480 | | 60 | 8.9860 |
| | 90 | 6.9150 | | 90 | 6.9706 |
| | 120 | 7.5220 | | 120 | 10.1165 |
| | 150 | 5.6627 | | 150 | 8.2932 |

3.2.3. Diurnal and Seasonal Variation of Semivariogram Parameters

The Range, the Sill and the Nugget effect, commonly known as the semivariogram parameters, play a key role in the Kriging interpolation process. To characterise these parameters over the East African low-latitude ionosphere with respect to TEC, their variations were studied in the meridional direction using the Gaussian model. Fig. 6 shows the diurnal and seasonal variation of these parameters during the year 2014.

The parameters were observed to vary with time of the day and seasons of the year. For instance, the highest values of the Range of lag distance exist between 04:00 UT - 09:00 UT throughout the year 2014 (panel (a)). During daytime, equinox months of the year 2014 registered the least values of Range between 09:00 UT and 16:00 UT, while the solstice months showed larger values of the Range around the same time. Particularly, the highest val-

ues of the Sill and the Nugget were observed during equinox months from 16:00 UT (19:00 LT) to 21:00 UT (00:00 LT). Amabayo et al. (2021) reported high Sill values from 17:00 UT to 20:00 UT when they modelled the spatial correlation of scintillation index (S4 proxy) values over the East African low-latitude region. They attributed the high Sill values to scintillation effects that occur from around 17:00 UT - 20:00 UT. However, the high Sill values observed in this study between 17:00 UT and 20:00 UT is attributed to large spatial-scale TEC variation of the low-latitude ionosphere. This could be as a result of latitudinal variation of TEC due to EIA. The EIA is characterised by the two humps of electron density on either side of the dip equator and a depleted region (trough) at the equator. This irregular latitudinal electron density distribution could be the cause of a larger variation of TEC in the meridional direction than in the zonal direction. The larger variation of TEC could be the main cause of the larger Sill values

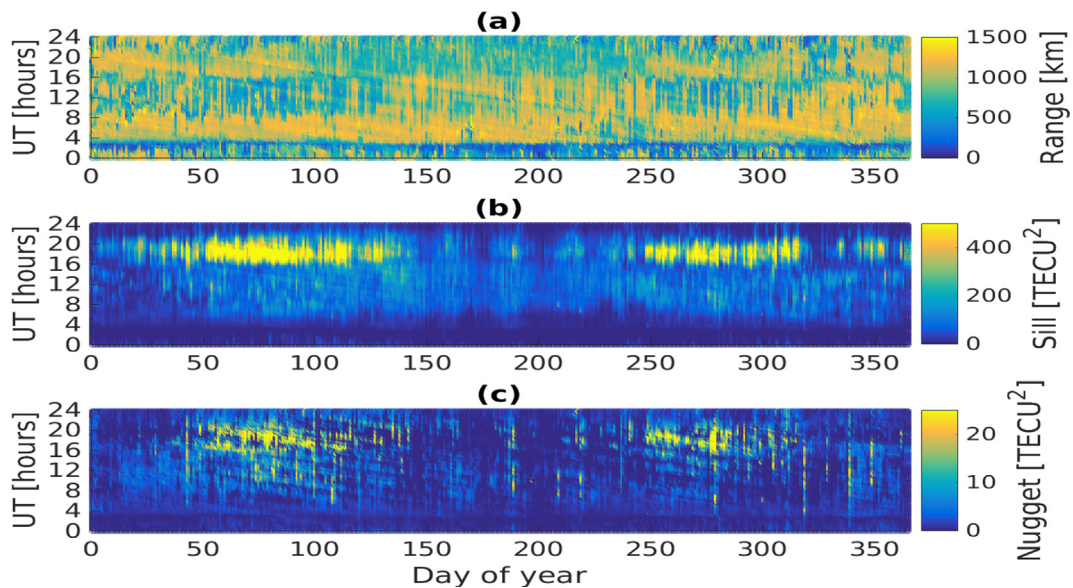


Fig. 6. Variation of the (a) Range, (b) Sill and (c) Nugget effect of TEC over the East African low-latitude region in the meridional direction. The values shown were determined at an interval of 15 min throughout the year 2014.

in the meridional direction because the Sill is a measure of variance. On the other hand, the Nugget effects are larger during equinox and smaller during solstice. The high nugget values are attributed to small spatial-scale TEC variation which could be as a result of ionospheric irregularities due to formation of plasma bubbles. The plasma bubbles usually occur after sunset and are believed to be caused mainly by Rayleigh–Taylor instabilities which begin from the bottom to the top side (F2-layer) of the ionosphere (Kelley, 2009). In Earlier studies, the occurrences of the low-latitude ionospheric irregularities were observed to be higher during equinox than in solstice (Paznukhov et al., 2012; Olwendo et al., 2013; Mungufeni et al., 2016; Akala et al., 2017; Andima et al., 2020). Therefore, the larger Nugget effects during equinoxes than in solstices could be due to the higher occurrences of the irregularities observed in the equinox as compared to solstice months.

The variation of the semivariogram parameters with time of the day and seasons of the year indicate the need to determine them dynamically every time the Kriging equation is solved to obtain the time-dependent Kriging weights. The calculated weights at a given instant were then used to perform the Kriging prediction of unmeasured values of TEC on regular grid points over the East African low-latitude on the selected days.

3.3. East African Ionospheric Maps

The regional TEC maps were generated by interpolating the VTEC values derived from the GNSS receivers at IPPs over the East African low-latitude region. The Gaussian semivariogram model parameters were used to compute and construct the Kriging TEC maps. The TEC maps were then compared with GIMs from CODE. For comparison purposes, the regional TEC map was constructed using

the same temporal resolution of 2 h as in CODE's data. Fig. 7 shows the TEC maps from Kriging and CODE over the East African low-latitude on DOY 075 of 2014 at 10:00 LT and 20:00 LT.

The results from Fig. 7 indicate that the regional TEC maps and CODE's GIMs captured well the development of EIA, though GIMs from CODE over smoothed the TEC values obtained from five IGS stations (ADIS, MBAR, MAL2, NURK and RCMN) sampled from the region. At 10:00 LT, CODE's GIMs predicted higher values of TEC than the Kriging regional TEC. These results show that the regional maps are more capable of reproducing the known features of the EIA. Therefore, the TEC maps constructed using the Kriging method can be used as a reliable technique in estimating the ionospheric TEC over the East African low-latitude region. In order to validate the TEC maps, the GPS VTEC values were compared with the VTEC values simulated from the limited measured VTEC. This was done for some selected PRNs that were visible at elevation angles greater than 30° on DOY 078 of 2014 from IGS receivers at ADIS, MBAR and MOIU.

The simulated values were at the IPP coordinates of the PRNs observed at the IGS receiver sites. Fig. 8 shows the results for PRN 2 at ADIS, PRN 17 at MBAR and PRN 14 at MOIU. These PRNs were selected to capture the performance of the Kriging VTEC compared to the measured values of GPS VTEC during day-time and night-time of DOY 078, 2014. The simulated VTEC values are in good agreement with the measured GPS VTEC from IGS receivers during both night and day. The maps were further validated by determining the Pearson's correlation coefficients between the Kriging VTEC and the measured GPS VTEC for all the visible PRNs on quiet DOY 078 and disturbed DOY 255 of 2014 at elevation angles greater than 30° . The TEC values corresponding to all the selected PRNs were first excluded before predicting them using the Krig-

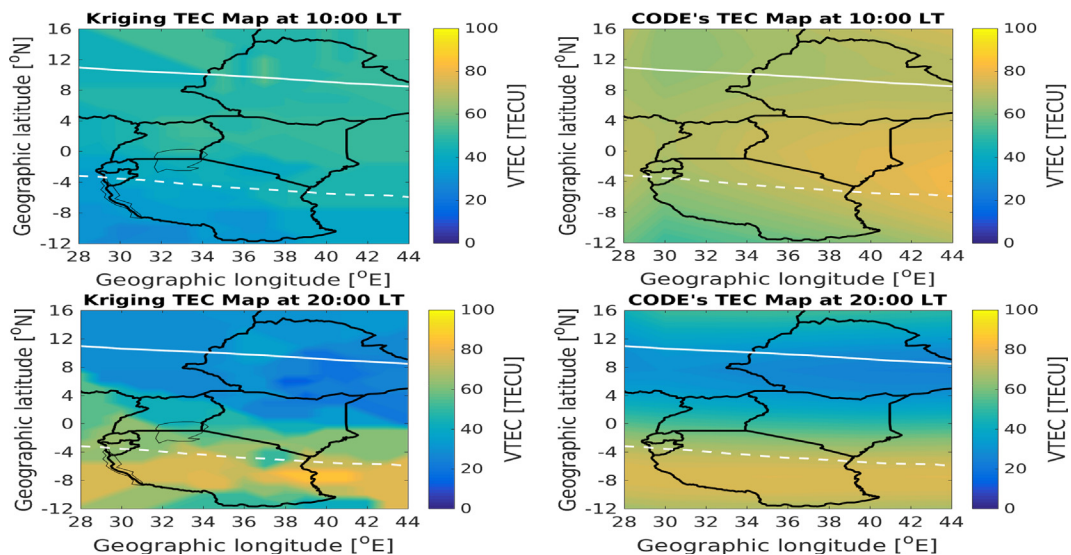


Fig. 7. Kriging TEC maps and CODE's GIMs over the East African low-latitude region on a typical quiet DOY 075 (16 March) 2014 at 10:00 LT and 20:00 LT. The solid white line is the magnetic (dip) equator (EIA trough) and the dotted white line is the southern EIA crest.

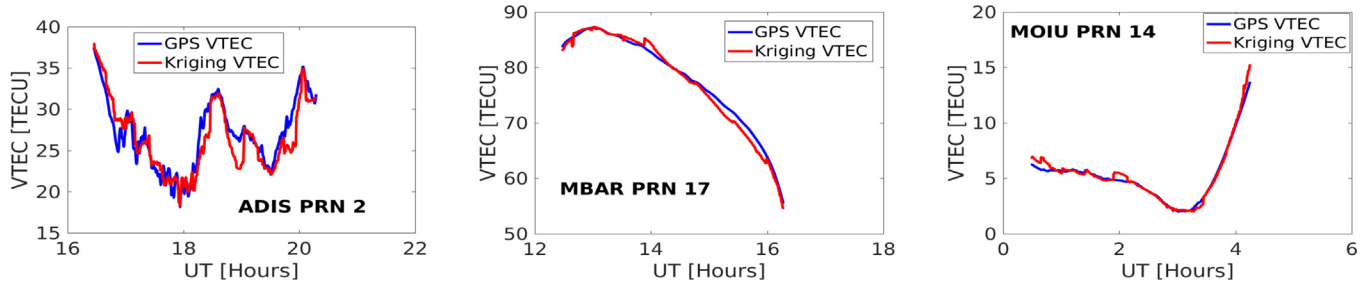


Fig. 8. Comparing Kriging VTEC with GPS VTEC over the stations ADIS, MBAR and MOIU for the selected PRNs on 19 March (DOY 078) 2014.

ing interpolation method. This was done to rule out the influence of the measured TEC values of a given PRN on the predicted TEC values.

Fig. 9 shows the results of the correlation analysis over the IGS stations of ADIS, MBAR and MOIU. The VTEC values interpolated by kriging method show a very high positive correlation with the measured GPS VTEC of coefficients between 0.9360 and 0.9970. This high positive correlation suggests that the constructed TEC maps provide good estimates for TEC at the unsampled locations over the East African low-latitude region, and may be useful in monitoring and understanding of the spatio-temporal variations of the regional ionosphere. The maps were also validated during geomagnetic storms over a single station as discussed in the following subsection.

3.3.1. Validation of TEC Maps over Malindi during Geomagnetic Storms

To validate the TEC maps during disturbed conditions, we compared the TEC maps predicted using Kriging method with GPS TEC, CODE's TEC and the background TEC (Quiet TEC) over Malindi (MAL2) as shown in Fig. 10. The CODE's TEC values over MAL2 were estimated using the nearest CODE's grid point of 40.0° longitude and -2.5° latitude at the IPPs of 350 km in altitude. Before using Kriging technique to predict the values of

TEC over MAL2, the measured TEC values for MAL2 IGS receiver station were first excluded for all the satellites visible by the station on the selected days for the storm. The background TEC were derived from three international quiet days of the month before the storm day.

Fig. 10 shows the variation of Kriging TEC, GPS TEC, CODE's TEC, Quiet TEC (Bottom panels) and the corresponding Dst index (Top panels) during the storms of 17th March, 2015 commonly known as the St. Patrick's day and 27th May, 2017. The GPS TEC was taken to represent the true state of the ionospheric TEC over Malindi.

Our regional TEC maps were used to predict ionospheric TEC over Malindi during the storm that occurred on St. Patrick's day. It was the strongest storm in the solar cycle 24 and it struck the Earth's magnetosphere at around 04:45 UT with a maximum Dst value of 45 nT at around 06:00 UT, and reached a minimum Dst value of -234 nT on 17th March, 2015 at around 23:00 UT. From Fig. 10 (a), the Kriging TEC maps show a very good agreement with the measured GPS TEC over Malindi from 16th – 19th March, 2015. However, it is observed that CODE's TEC maps predicted slightly higher values of TEC than the GPS TEC during the storm period from 16th – 19th March, 2015. The Kriging TEC values were much lower than the background TEC on 18th and 19th March, 2015. This shows that the storm resulted in a strong

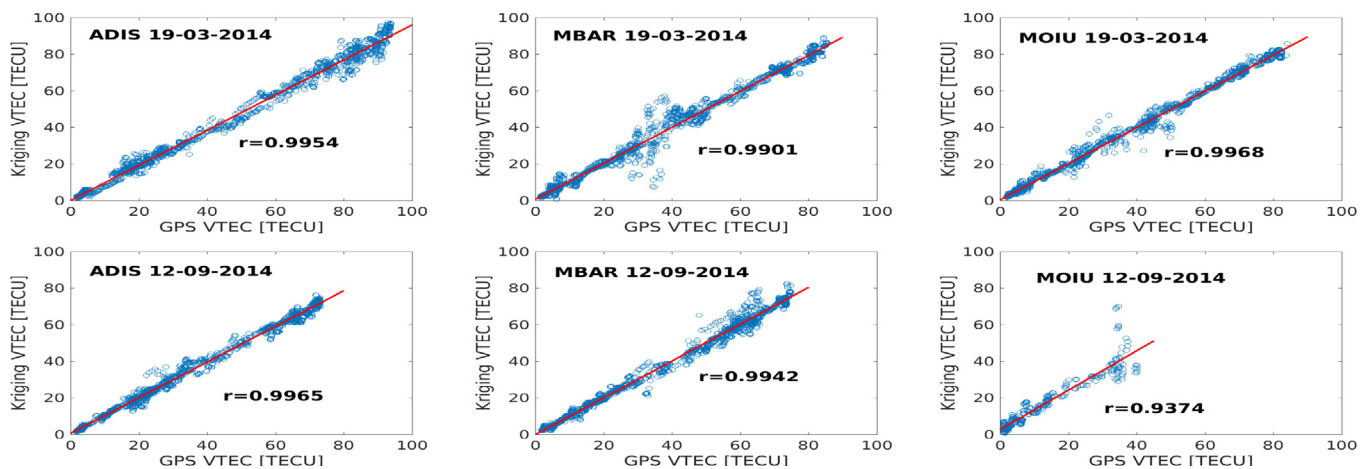


Fig. 9. Correlation analysis between Kriging VTEC and the GPS VTEC over the stations ADIS, MBAR and MOIU for all the PRNs on quiet and disturbed days of 19 March (DOY 078) and 12 September (DOY 255) of 2014 respectively. The red lines are the lines of best fit.

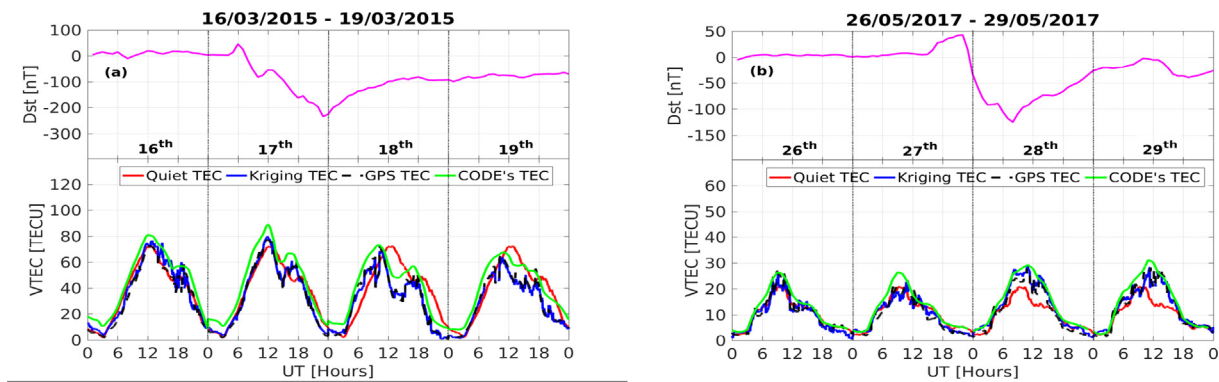


Fig. 10. Variation of Kriging TEC, GPS TEC, CODE's TEC and Quiet TEC over Malindi during the geomagnetic storms of (a) 17th March, 2015 and (b) 27th May, 2017.

suppression of the ionospheric TEC during the recovery phase, indicating that the storm had negative impacts on the ionosphere over Malindi during the recovery period. The negative impacts of the same storm on 18th and 19th March, 2015 were reported over Brazilian sector by [Fagundes et al. \(2016\)](#). [Olwendo et al. \(2016\)](#) also reported very strong negative impacts of the storm over the East African ionosphere during recovery phase for stations away from the magnetic equator.

The Kriging TEC maps were also used to predict the ionospheric state over Malindi during another moderate storm which occurred on 27th May, 2017 at about 16:00 UT. This storm had a minimum Dst value of -125 nT on 28th May, 2017 at about 08:00 UT. The TEC values predicted by Kriging approach show a very good agreement with GPS TEC and CODE's TEC. The CODE's GIMs predicted the disturbed TEC of May 2017 better than the disturbed TEC of March 2015. According to [Andima et al. \(2019\)](#), GIMs from CODE over estimated disturbed TEC during HSA year and gave good predictions of disturbed TEC for LSA year. Our regional maps performed quite well during both HSA and LSA years. [Fig. 10\(b\)](#) shows that the Kriging TEC values were higher than the Quiet TEC values on 28th and 29th May, 2017, which is an indication that the storm resulted in TEC enhancement over Malindi during the recovery phase. [Chakraborty et al. \(2020\)](#) also reported enhancement in TEC values on 28th and 29th May, 2017 when they studied the effects of the same storm on the ionosphere over the Indian sector. Generally, the TEC maps constructed using Kriging method predicted the GPS TEC over Malindi better than the CODE's TEC maps during disturbed conditions. Therefore, the Kriging TEC maps can give a good estimate of the GPS TEC over the East African low-latitude region.

4. Conclusion

In this work, we modelled the spatial correlation of TEC using a semivariogram model and constructed the TEC maps over the East African low-latitude region. Before

constructing the maps, the behaviour of TEC over this region was characterised using data for 2014 and 2018 during quiet and disturbed conditions. The key findings of the study can be summarised as follows: (i) Higher values of TEC were observed during March equinox than September equinox, suggesting the existence of equinoctial asymmetry of TEC over the region. (ii) PRE at the crest occurs about an hour earlier than that at the trough. The PREs occurred during equinoctial months of 2014 between 18:00 UT and 21:00 UT. (iii) The best semivariogram model to describe the spatial variation of TEC over the East African low-latitude region is the Gaussian model. (iv) The results indicate that the spatial variation of TEC is larger in the meridional direction than in the zonal direction. This is attributed to EIA which forces ionospheric plasma to diffuse in the meridional direction, forming a low electron density region at the trough (dip equator) and high electron density regions at the EIA crests. (v) The regional maps gave better estimates of the GPS-derived TEC during quiet and disturbed conditions compared to the estimates from the CODE's GIMs over the region. This suggests that the Kriging TEC maps can be used as a good tool for predicting TEC over the East African low-latitude region where the GPS receivers are still sparse.

Declaration of Competing Interest

The authors declare that they have no known competing financial interests or personal relationships that could have appeared to influence the work reported in this paper.

Acknowledgement

The authors acknowledge financial support from Swedish International Development Agency (SIDA) through the International Science Programme (ISP) of Uppsala University in Sweden.

We also thank the University Navstar Consortium (UNAVCO) for providing the GPS-TEC data used in this study.

References

- Akala, A.O., Ejalonibu, A.H., Doherty, P.H., Radicella, S.M., Groves, K.M., Carrano, C.S., Bridgwood, C.T., Stoneback, R.A., 2017. Characterization of GNSS amplitude scintillations over Addis Ababa during 2009–2013. *Adv. Space Res.* 59, 1969–1983. <https://doi.org/10.1016/j.asr.2017.01.044>.
- Amabayo, E.B., Andima, G., Ssenyunzi, R.C., 2021. Instantaneous ionospheric scintillation mapping over the East African region by use of GPS derived amplitude scintillation proxy. *Asian J. Res. Rev. Phys.* 6–20. <https://doi.org/10.9734/AJR2P/2021/v4i230138>.
- Anderson, D.N., Mendillo, M., Herniter, B., 1987. A semi-empirical low-latitude ionospheric model. *Radio Sci.* 22, 292–306.
- Andima, Geoffrey, Amabayo, Emirant B., Jurua, Edward, Cilliers, Pierre J., 2020. GPS derived amplitude scintillation proxy model: A case over a low latitude station in East Africa. *J. Atmosph. Sol.-Terrestrial Phys.* 211, 105461.
- Andima, G., Amabayo, E.B., Jurua, E., Cilliers, P.J., 2019. Modeling of GPS total electron content over the African low-latitude region using empirical orthogonal functions. *Annales Geophysicae. Copernicus GmbH*, pp. 65–76.
- Appleton, E.V., 1946. Two anomalies in the ionosphere. *Nature* 157, 691.
- Arikan, F., Yilmaz, A., Arikan, O., Sayin, I., Gurun, M., Akdogan, K., Yildirim, S., 2009. Space weather activities of ionolab group: TEC mapping. In: EGU General Assembly Conference Abstracts, p. 6962.
- Bagiya, M.S., Joshi, H., Iyer, K., Aggarwal, M., Ravindran, S., Pathan, B., 2009. TEC variations during low solar activity period (2005–2007) near the equatorial ionospheric anomaly crest region in India. In: *Annales Geophysicae, Copernicus GmbH*. pp. 1047–1057. <https://doi.org/10.5194/angeo-27-1047-2009>.
- Bailey, G., Su, Y., Oyama, K.I., 2000. Yearly variations in the low-latitude topside ionosphere. *Annales Geophysicae. Copernicus GmbH*, pp. 789–798. <https://doi.org/10.1007/s00585-000-0789-0>.
- Bilitza, D., Brown, S.A., Wang, M.Y., Souza, J.R., Roddy, P.A., 2012. Measurements and IRI model predictions during the recent solar minimum. *J. Atmos. Solar Terr. Phys.* 86, 99–106.
- Biswas, Asim, Si, Bing Cheng, 2013. Model averaging for semivariogram model parameters. *Adv. Agrophys. Res.* 4, 81–96. <https://doi.org/10.5772/52339>.
- Blanch, J., Walter, T., 2002. Application of spatial statistics to ionosphere estimation for WAAS. In: *Proceedings of the 2002 National Technical Meeting of The Institute of Navigation*, pp. 719–724.
- Chakraborty Sumanjit, Ray Dibyendu Datta, Abhirup Paul, Ashik. 2020. Effects of CME and CIR induced geomagnetic storms on low-latitude ionization over Indian longitudes in terms of neutral dynamics. *Adv. Space Res.* 120(1), 198–213, Elsevier.
- Chen, Z., Zhang, S.R., Coster, A.J., Fang, G., 2015. EOF analysis and modeling of GPS TEC climatology over North America. *J. Geophys. Res.: Space Phys.* 120, 3118–3129.
- Cressie, N.A., 1993. *Statistics for Spatial Data*. John Wiley & Sons. Inc. [Google Scholar], New York.
- Deutsch, C.V., 1998. *GSLIB: Geostatistical Software Library and User's Guide: Buch*. Oxford University Press.
- Fagundes, P.R., Cardoso, F.A., Fejer, B.G., Venkatesh, K., Pillat, V.G. 2016. Positive and negative GPS-TEC ionospheric storm effects during the extreme space weather event of March 2015 over the Brazilian sector. *J. Geophys. Res.: Space Phys.* 121(6), 5613–5625, Wiley Online Library. <https://doi.org/10.1002/2015JA022214>.
- Gade, K., 2010. A non-singular horizontal position representation. *J. Navigat.* 63, 395–417.
- Ghosh, P., Otsuka, Y., Mani, S., Shinagawa, H., 2020. Day-to-day variation of pre-reversal enhancement in the equatorial ionosphere based on GAIA model simulations. *Earth, Planets Space* 72, 1–8.
- Gopi, S, 2010. *Rinex GPS-TEC program, version 1.45*. Boston College.
- Grynshyna-Poliuga, O., 2019. Characteristic of modelling spatial processes using geostatistical analysis. *Adv. Space Res.* 64, 415–426.
- Grynshyna-Poliuga, O., Stanislawska, I., Swiatek, A., 2014. Regional ionosphere mapping with kriging and B-spline methods. In: *Mitigation of Ionospheric Threats to GNSS: an Appraisal of the Scientific and Technological Outputs of the TRANSMIT Project*. IntechOpen.
- Hajra, R., Chakraborty, S.K., Tsurutani, B.T., DasGupta, A., Echer, E., Brum, C.G., Gonzalez, W.D., Sobral, J.H.A., 2016. An empirical model of ionospheric total electron content (TEC) near the crest of the equatorial ionization anomaly (EIA). *J. Space Weather Space Climate* 6, A29.
- Hanson, W., Nagy, A., 1966. Rj mo ett. Ionization transport effects in the equatorial F region. *J. Geophys. Res* 71, 5559–5572.
- Heelis, R., Crowley, G., Rodrigues, F., Reynolds, A., Wilder, R., Azeem, I., Maute, A., 2012. The role of zonal winds in the production of a pre-reversal enhancement in the vertical ion drift in the low latitude ionosphere. *J. Geophys. Res.: Space Phys.* 117.
- Jin, S.G., Wang, J., Zhang, H.p., Zhu, W.Y., 2004. Real-time monitoring and prediction of ionospheric electron content by means of GPS. *Chinese Astron. Astrophys.* 28, 331–337.
- Kelley, M.C., 2009. *The Earth's Ionosphere: Plasma Physics and Electrodynamics*. Academic Press.
- Kitanidis, P.K., 1997. *Introduction to Geostatistics: Applications in Hydrogeology*. Cambridge University Press.
- Lichtenstern, A, 2013. *Kriging methods in spatial statistics*.
- Mannucci, A., Wilson, B., Yuan, D., Ho, C., Lindqwister, U., Runge, T., 1998. A global mapping technique for GPS-derived ionospheric total electron content measurements. *Radio Sci.* 33, 565–582.
- Martyn, D.F., 1947. Atmospheric tides in the ionosphere-i. solar tides in the F2 region. *Proc. Roy. Soc. London. Series A. Mathe. Phys. Sci.* 189, 241–260.
- Matheron, G., 1963. Principles of geostatistics. *Econ. Geol.* 58, 1246–1266.
- Mengist, C.K., Kim, Y.H., Yeshita, B.D., Workayehu, A.B., 2016. Mapping the East African ionosphere using ground-based GPS TEC measurements. *J. Astron. Space Sci.* 33, 29–36.
- Mitra, S., 1946. Geomagnetic control of region F2 of the ionosphere. *Nature* 158, 668–669.
- Mungufeni, Patrick, Habarulema, John Bosco, Jurua, Edward, 2016. Trends of ionospheric irregularities over African low latitude region during quiet geomagnetic conditions. *J. Atmosph. Sol.-Terrestrial Phys.* 138, 261–267.
- Norsuzila, Y., Abdullah, M., Ismail, M., 2010. GPS total electron content (TEC) prediction at ionosphere layer over the equatorial region. In: *Trends in Telecommunications Technologies*. IntechOpen.
- Olwendo, O.J., Baluku, T., Baki, P., Cilliers, P.J., Mito, C., Doherty, P., 2013. Low latitude ionospheric scintillation and zonal irregularity drifts observed with GPS-SCINDA system and closely spaced VHF receivers in Kenya. *Adv. Space Res.* 51, 1715–1726.
- Olwendo, O., Yamazaki, Y., Cilliers, P., Baki, P., Doherty, P., 2016. A study on the variability of ionospheric total electron content over the East African low-latitude region and storm time ionospheric variations. *Radio Sci.* 51, 1503–1518.
- Orús, R., Hernández-Pajares, M., Juan, J., Sanz, J., 2005. Improvement of global ionospheric $\sqrt{\text{TEC}}$ maps by using kriging interpolation technique. *J. Atmos. Solar Terr. Phys.* 67, 1598–1609.
- Pignalberi, A., Pietrella, M., Pezzopane, M., Rizzi, R., 2018. Improvements and validation of the iri up method under moderate, strong, and severe geomagnetic storms. *Earth, Planets Space* 70, 1–22.
- Paznukhov, V.V., Carrano, C.S., Doherty, P.H., Groves, K.M., Caton, R. G., Valladares, C.E., Seemala, G.K., Bridgwood, C.T., Adeniyi, J., Amaeshi, L.L.N., et al. 2012. Equatorial plasma bubbles and L-band scintillations in Africa during solar minimum. In: *Annales Geophysicae, Copernicus GmbH*.30, pp. 675–682.
- Rama Rao, P.V.S., Niranjana, K., Prasad, D.S.V.V., Gopi Krishna, S., Uma, G., 2006. On the validity of the ionospheric pierce point (IPP) altitude of 350 km in the Indian equatorial and low-latitude sector. *Ann. Geophys.* 24, 2159–2168.

- Sayin, I., Arikan, F., Arikan, O., 2008. Regional TEC mapping with random field priors and kriging. *Radio Sci.* 43.
- Schmidt, M., Dettmering, D., Mößner, M., Wang, Y., Zhang, J., 2011. Comparison of spherical harmonic and B-spline models for the vertical total electron content. *Radio Sci.* 46.
- Seemala, G., Valladares, C., 2011. Statistics of total electron content depletions observed over the South American continent for the year 2008. *Radio Sci.* 46 (5). <https://doi.org/10.1029/2011RS004722>.
- Stanislawska, I., Juchnikowski, G., Cander, L.R., Ciraolo, L., Bradley, P., Zbyszynski, Z., Swiatek, A., 2002. The kriging method of TEC instantaneous mapping. *Adv. Space Res.* 29, 945–948.
- Sulungu, E.D., Uiso, C.B., Sibanda, P., 2018. Total electron content derived from global positioning system during solar maximum of 2012–2013 over the eastern part of the African sector. *Tanzania J. Sci.* 44, 62–74.
- Tariku, Y.A., 2015. Patterns of GPS-TEC variation over low-latitude regions (African sector) during the deep solar minimum (2008 to 2009) and solar maximum (2012 to 2013) phases. *Earth, Planets Space* 67, 1–9.
- Webster, R., Oliver, M., 2001. Local estimation or prediction: kriging. *Geostatistics Environ. Sci.*, 153–194
- Wielgosz, P., Grejner-Brzezinska, D., Kashani, I., 2003. Regional ionosphere mapping with kriging and multiquadric methods. *J. Global Position. Syst.* 2, 48–55.
- Zewdie, G.K., 2012. Tomographic imaging of ionospheric electron density over Ethiopia using ground based GPS receivers. no. June, 112.